Subfilter scalar-flux vector orientation in homogeneous isotropic turbulence

Siddhartha Verma*
Graduate Aerospace Laboratories, California Institute of Technology, Pasadena, California, USA

G. Blanquart†
Department of Mechanical Engineering, California Institute of Technology, Pasadena, California, USA

(Received 28 February 2014; published 24 June 2014)

The geometric orientation of the subfilter-scale scalar-flux vector is examined in homogeneous isotropic turbulence. Vector orientation is determined using the eigenframe of the resolved strain-rate tensor. The Schmidt number is kept sufficiently large so as to leave the velocity field, and hence the strain-rate tensor, unaltered by filtering in the viscous-convective subrange. Strong preferential alignment is observed for the case of Gaussian and box filters, whereas the sharp-spectral filter leads to close to a random orientation. The orientation angle obtained with the Gaussian and box filters is largely independent of the filter width and the Schmidt number. It is shown that the alignment direction observed numerically using these two filters is predicted very well by the tensor-diffusivity model. Moreover, preferred alignment of the scalar gradient vector in the eigenframe is shown to mitigate any probable issues of negative diffusivity in the tensor-diffusivity model. Consequentially, the model might not suffer from solution instability when used for large eddy simulations of scalar transport in homogeneous isotropic turbulence. Further *a priori* tests indicate poor alignment of the Smagorinsky and stretched vortex model predictions with the exact subfilter flux. Finally, strong filter dependence of subfilter scalar-flux orientation suggests that explicit filtering may be preferable to implicit filtering in large eddy simulations.

DOI: 10.1103/PhysRevE.89.063015 PACS number(s): 47.27.ep, 47.27.Gs

I. INTRODUCTION

Direct numerical simulation (DNS) of turbulent mixing at very high Reynolds and Schmidt numbers is challenging due to high computational cost. The Schmidt number, defined as the ratio of the kinematic viscosity of fluid to the molecular diffusivity of the scalar ($\mathrm{Sc} = \nu/\mathcal{D}$), determines the smallest length scales that are important for scalar transport. For $\mathrm{Sc} \gg 1$, the smallest scalar length scales (called the Batchelor scale, η_B [1]) are much smaller than the smallest velocity length scales (Kolmogorov scale, η). Resolving all of these relevant length scales in simulations becomes unmanageable.

Large eddy simulations (LES) try to reduce computational cost in such flows to manageable levels by resolving the larger length scales to a certain extent and employing models to represent the dynamics of the smaller, unresolved scales. The mathematical term to be modeled in LES of scalar transport, referred to as the subfilter-scale scalar flux (SFF), is obtained by applying a homogeneous spatial filtering operation ($\widetilde{\cdot}$) to the convection-diffusion equation,

$$\frac{\partial \phi}{\partial t} + \boldsymbol{\nabla} \cdot (\boldsymbol{u}\phi) = \mathcal{D}\nabla^2 \phi, \tag{1}$$

leading to

$$\frac{\partial \widetilde{\phi}}{\partial t} + \boldsymbol{\nabla} \cdot (\widetilde{\boldsymbol{u}}\widetilde{\phi}) = \mathcal{D}\nabla^2 \widetilde{\phi} - \boldsymbol{\nabla} \cdot \boldsymbol{\tau}_\phi, \tag{2}$$

$$\boldsymbol{\tau}_\phi = \widetilde{\boldsymbol{u}\phi} - \widetilde{\boldsymbol{u}}\widetilde{\phi}. \tag{3}$$

Here, $\boldsymbol{\tau}_\phi$ is the SFF vector and encapsulates the effects of nonlinear interactions among the resolved and unresolved length scales. A promising framework to reduce the cost of numerical simulations for $\mathrm{Sc} \gg 1$, and still retain most of the relevant nonlinear interactions, is to place the LES filter cutoff in the viscous-convective subrange [2,3]. Under these conditions, the velocity field is fully resolved and only the scalar field is filtered.

A variety of models are available in the literature for emulating $\boldsymbol{\tau}_\phi$, namely, variations of the Smagorinsky model [4], the stretched vortex model [5], the similarity model [6,7], and the tensor-diffusivity model [8–11]. These models usually rely on observed, or hypothesized, behavior of the subfilter scalar-flux vector in filtered experimental or numerical simulation data. Unfortunately, the models were designed primarily for filtering in the inertial subrange and remain largely untested in the viscous-convective subrange. One of the important properties of these models that must be tested is the predicted orientation of the $\boldsymbol{\tau}_\phi$ vector. Accurate knowledge of this orientation is crucial for correctly determining the amount of subfilter scalar variance dissipation given by

$$\chi_{\boldsymbol{\tau}_\phi} = -2\boldsymbol{\tau}_\phi \cdot \boldsymbol{\nabla}\phi. \tag{4}$$

Given the critical role of $\boldsymbol{\tau}_\phi$ orientation in regulating subfilter dissipation [Eq. (4)], the objective of the present work is to investigate the vector's alignment behavior in homogeneous isotropic turbulence. More precisely, the goals are threefold: (1) to relate the predicted vector's orientation to known velocity-dependent quantities; (2) to identify the influence (if any) of the Schmidt number of the transported scalar and the influence of width and shape of the filtering kernel used; and (3) to assess the ability of various existing models in predicting this orientation. In the scope of reducing the cost of LES for high Schmidt number scalar transport, the present analysis focuses primarily on scenarios involving filter-width location in the viscous-convective subrange.

*sverma@caltech.edu
†g.blanquart@caltech.edu

The remainder of the paper is structured as follows. Details of the simulations used for *a priori* analysis are provided in Sec. II. Section III examines the preferential alignment of the vorticity vector ($\boldsymbol{\omega}$), the scalar gradient vector ($\nabla\phi$), and the numerically computed SFF vector ($\boldsymbol{\tau}_\phi$) in the strain-rate eigenframe. The accuracy with which various subfilter models predict the orientation of $\boldsymbol{\tau}_\phi$ is discussed in Sec. IV. Section V details the mathematical analysis of the tensor-diffusivity model, which is used to explain the preferential alignment observed in Sec. III. Finally, the effects of filter shape and scalar-forcing method on $\boldsymbol{\tau}_\phi$ orientation, and the ensuing implications of using implicit filtering in LES, are discussed in Sec. VI.

II. SIMULATION DETAILS

To investigate *a priori* the behavior of the orientation of the computed SFF vector, direct numerical simulations of homogeneous isotropic turbulence are used. The simulations were performed using a second-order energy-conserving finite-difference velocity scheme [12], and a fifth-order accurate upwind finite-volume scheme for the scalar [13]. The velocity field was forced by injecting energy in a low-wave-number shell [14]. Two distinct scalar-forcing techniques were used, one characterized by the presence of a mean scalar gradient (MSG) [15] and the other simulating the decay of scalar fluctuations (linear scalar forcing, LS) [16]. The use of the two scalar-forcing methods allows us to investigate differences in $\boldsymbol{\tau}_\phi$ alignment that might be related to distinct scalar variance cascade mechanisms (forced vs decaying) at the small length scales. Simulations using both MSG and LS forcings were run simultaneously; two independent scalars were transported using the same velocity field, each being forced using one of the forcing methods.

Details of the physical parameters used in the simulations are given in Table I. The Taylor-scale Reynolds number for all the simulations was kept constant at a value of $\mathrm{Re}_\lambda = 30$, and the Schmidt number was varied from $\mathrm{Sc} = 4$ to $\mathrm{Sc} = 256$. It was necessary to restrict Re_λ to a relatively low value, since resolving the Batchelor scale at high Sc incurs considerable computational cost. Nonetheless, scalar transport in the viscous-convective subrange is governed largely by the velocity scales in the dissipative range, which show universal behavior to some extent even at low Reynolds numbers [17]. $\mathrm{Re}_\lambda = 30$ yields a sufficiently turbulent flow field for our purpose, and most of the results discussed in this paper may be extended to larger Reynolds numbers with appropriate consideration.

For postprocessing purposes, scalar and velocity modes corresponding to the highest two-thirds of the wave numbers were deleted using a sharp-spectral filter to prevent aliasing caused by multiplication of variables (Orszag' s two-thirds truncation rule [18]).

TABLE I. DNS datasets used for analyzing $\boldsymbol{\tau}_\phi$ behavior ($\mathrm{Re}_\lambda = 30$).

Case	N	Sc	$\kappa_{\max}\eta$	$\kappa_{\max}\eta_B$
A	1024	256	23.2	1.4
B	512	16	11.6	2.9
C	512	4	11.6	5.8

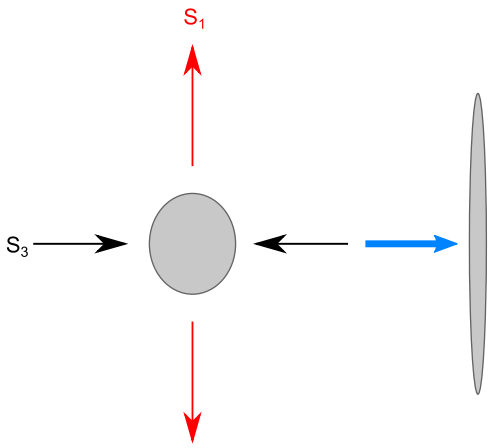

FIG. 1. (Color online) Schematic of scalar material element undergoing straining.

III. VECTOR ALIGNMENT IN THE LOCAL STRAIN-RATE EIGENFRAME

A. Choice of reference frame

Inspecting the orientation of the various vectors of interest (e.g., $\boldsymbol{\omega}$, $\nabla\phi$, $\boldsymbol{\tau}_\phi$) requires the selection of an appropriate reference frame. The laboratory-fixed frame is not an ideal choice for this purpose, since the homogeneous and isotropic nature of the turbulent fluctuations results in random orientation of the vectors with respect to the laboratory-based orthonormal axes. Instead, the orthonormal reference frame formed by the eigenvectors of the local strain-rate tensor [$S_{ij} = \frac{1}{2}(u_{i,j} + u_{j,i})$] presents a more suitable choice [19,20]. This is due to the fact that the dynamics of passive scalar transport (as well as those of the velocity field itself) are governed largely by straining from the velocity field. Additionally, the tensor-diffusivity model depends closely on vorticity and the velocity strain rate (as will become apparent in Sec. V), which provides further motivation for using the eigenframe as a basis for determining vector orientation.

Figure 1 shows the schematic of a scalar material element undergoing deformation in a straining flow field. S_1 represents the direction of the most extensive eigenvector of S_{ij} (positive eigenvalue: $\lambda_1 > 0$), and S_3 represents the direction of the most compressive one ($\lambda_3 < 0$). The intermediate eigenvalue (corresponding to the eigenvector S_2) is known to be close to zero (and slightly positive) from experimental [21] and numerical studies [19] of incompressible homogeneous isotropic turbulence. Thus, the S_2 direction experiences comparatively little material element deformation.

B. Alignment of $\boldsymbol{\omega}$ and $\nabla\boldsymbol{\phi}$ in the eigenframe

To examine the preferential alignment of the various quantities of interest, we make use of three-dimensional (3D) joint probability density functions (PDF), hereafter referred to as sphere PDFs. Such illustrations, e.g., the ones shown in Fig. 2 for the vorticity vector ($\boldsymbol{\omega} = \boldsymbol{\nabla} \times \boldsymbol{u}$) and the scalar

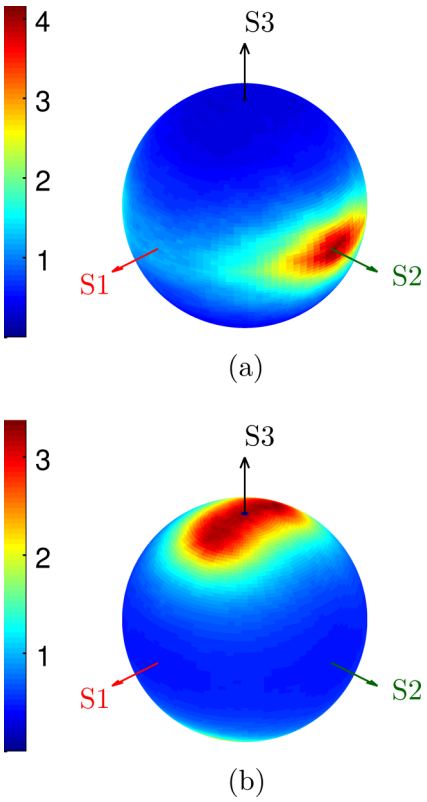

FIG. 2. (Color online) Alignment of (a) $\boldsymbol{\omega}$ and (b) $\nabla\phi$ in the S_{ij} eigenframe. (Case A: $\mathrm{Re}_\lambda = 30$, $\mathrm{Sc} = 256$).

gradient vector ($\nabla\phi$), provide a powerful means of visualizing vector orientation in the strain-rate eigenframe [20,22]. The color levels denote the probability density function of vector orientation, normalized by the PDF value for uniform random orientation ($\mathrm{PDF}_{\mathrm{random}} = 1/(4\pi) = 0.0796$). In other words, a value of 1 on the color axis denotes probability equal to that of random orientation, a value lower than 1 indicates aversion to alignment at the corresponding locations, and a value greater than 1 suggests preferred orientation.

Both $\boldsymbol{\omega}$ and $\nabla\phi$ are known to exhibit strong preferential orientation in the S_{ij} eigenframe, with the vorticity vector aligning along the intermediate eigenvector S_2 [19,21–24] [Fig. 2(a)], and the scalar gradient vector aligning with the most compressive eigenvector S_3 [19] [Fig. 2(b)]. It is evident from Fig. 2(a) that the probability of alignment of $\boldsymbol{\omega}$ along the S_2 axis is approximately 4 times higher than would be expected for random orientation and falls quickly to values close to 0 in regions far away from the axis. The scalar gradient [Fig. 2(b)] tends to align along the S_3 axis with a normalized PDF value slightly greater than 3. The alignment of $\nabla\phi$ with S_3 is an expected physical outcome and may be explained using Fig. 1; compression of the material element in the S_3 direction gives rise to the highest scalar gradient magnitude in this direction.

C. Alignment of $\boldsymbol{\tau}_\phi$ in the eigenframe

To inspect the alignment of $\boldsymbol{\tau}_\phi$, the appropriate terms in Eq. (3) are obtained by filtering the DNS datasets spatially. This operation corresponds to a convolution with a filtering kernel in physical space, or equivalently, multiplication in Fourier space. Three different filtering kernels, namely the Gaussian filter, the box (or top-hat) filter, and the sharp-spectral filter are used here. The respective kernel representations in physical space are given below [8]:

$$\text{Gaussian: } G(x) = \left(\frac{6}{\pi\Delta^2}\right)^{\frac{1}{2}} \exp\left(-\frac{6x^2}{\Delta^2}\right), \tag{5}$$

$$\text{Box: } G(x) = \frac{1}{\Delta} H\left(\frac{\Delta}{2} - |x|\right), \tag{6}$$

$$\text{Sharp: } G(x) = \frac{\sin(\pi x/\Delta)}{\pi x}. \tag{7}$$

Here, Δ is referred to as the filterwidth. The forms of the Gaussian and top-hat filters in Eqs. (5) and (6) ensure that their second moments ($\int_{-\infty}^{\infty} x^2 G(x)dx$) match [8]. The width (in physical space) for the sharp filter is defined through the filter cutoff wave number ($\kappa_c = \pi/\Delta$) in Fourier space. In most of the analysis shown in this paper, Δ has been chosen such that the effective filter cutoff wave number lies in the viscous-convective subrange; in other words, $\kappa_c\eta > 1.5$.

Figure 3 shows the sphere PDF for $\boldsymbol{\tau}_\phi$ in the eigenframe, computed pointwise for case A ($\mathrm{Re}_\lambda = 30$, $\mathrm{Sc} = 256$) using the Gaussian filter. The panels show the alignment behavior for three different effective filter widths, corresponding to a scenario when approximately 60% ($\kappa_c\eta_B = 0.625$), 93% ($\kappa_c\eta_B = 0.1$), and 97% ($\kappa_c\eta_B = 0.05$) of the scalar modes have been filtered out. At these cutoff widths, $\boldsymbol{\tau}_\phi$ exhibits strong preference for alignment at a particular angle in the

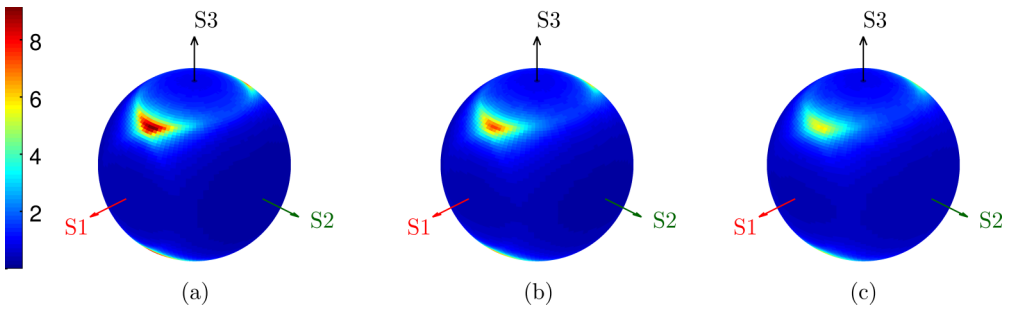

FIG. 3. (Color online) Alignment of the subfilter flux vector ($\boldsymbol{\tau}_\phi$) in the filtered strain-rate ($\widetilde{S}_{ij}$) eigenframe, computed from case A using the Gaussian filtering kernel. Figures shown correspond to three different filter cutoffs: (a) $\kappa_c\eta = 10$, $\kappa_c\eta_B = 0.625$; (b) $\kappa_c\eta = 1.6$, $\kappa_c\eta_B = 0.1$; and (c) $\kappa_c\eta = 0.8$, $\kappa_c\eta_B = 0.05$.

TABLE II. PDFs of SFF vector alignment for different Schmidt numbers, using the Gaussian filtering kernel. The ranges of accuracy for θ_P and θ_A are $\pm 0.9^\circ$ and $\pm 1.8^\circ$, respectively, since 100 bins were used for discretizing both of these angles when constructing the sphere PDFs.

	Case A (Sc = 256)			Case B (Sc = 16)			Case C (Sc = 4)		
PDF	$\kappa_c\eta = 10$	$\kappa_c\eta = 1.6$	$\kappa\eta = 0.8$	$\kappa_c\eta = 3.2$	$\kappa_c\eta = 1.6$	$\kappa_c\eta = 0.8$	$\kappa_c\eta = 1.8$	$\kappa_c\eta = 1.6$	$\kappa_c\eta = 0.8$
min	0.15	0.17	0.18	0.14	0.14	0.15	0.14	0.14	0.13
max	9.14	7.32	5.77	9.57	8.57	7.09	8.91	8.75	7.10
θ_P	42.3°	42.3°	42.3°	40.5°	40.5°	40.5°	40.5°	40.5°	40.5°
θ_A	5.4°	1.8°	5.4°	−1.8°	−1.8°	−1.8°	1.8°	1.8°	1.8°

S_1-S_3 plane, specifically, at a polar angle of $41.4^\circ \pm 1.8^\circ$ from the S_3 axis. The normalized PDF maxima are 9.14, 7.32, and 5.77 times the value expected for random orientation, respectively. It is surprising to observe such large values of PDF_{max}, especially in cases where more than 90% of the scalar modes present originally have been filtered out [Figs. 3(b) and 3(c)]. Nonetheless, there is a noticeable drop in the value of PDF_{max} with increasing filter-width size.

We note that the velocity field (and hence $\widetilde{S}_{ij}$) is fully resolved for the first two panels ($\kappa_c\eta = 10$ and 1.6) and only marginally filtered for the last one ($\kappa_c\eta = 0.8$). This happens since filtering in the viscous-convective subrange (feasible only for $\text{Sc} \gg 1$: Table I) does not impact the velocity field, as long as $\kappa_c\eta \geqslant 1.5$. The same argument would not hold for $\text{Sc} \leqslant 1$, since cutoffs with $\kappa_c\eta \leqslant 1.5$ would result in both scalar and velocity modes being filtered.

Sphere PDFs for all the datasets listed in Table I were computed in a similar manner, and the relevant quantitative data are listed in Table II. We use θ_P to denote the polar angle measured from axis S_3 to the location of PDF_{max} on the sphere PDFs, and θ_A to represent the corresponding azimuthal angle measured from axis S_1. For enhanced readability, all angles have been confined using symmetry to the quadrant that is prominently visible in Fig. 3; i.e., we set $\theta_P = 180^\circ - \theta_P$ if $\theta_P > 90^\circ$, $\theta_A = \theta_A - 180^\circ$ if $90^\circ < \theta_A \leqslant 270^\circ$, and $\theta_A = \theta_A - 360^\circ$ if $\theta_A > 270^\circ$. θ_P values for all three cases (A through C in Table II) are observed to be $41.4^\circ \pm 1.8^\circ$, and θ_A values fall within the range $1.8 \pm 5.4^\circ$. The angles, as well as the PDF max/min data, show little variation among the three cases, which points to possible Schmidt number independence of the SFF vector orientation. This observation, as well as the weak influence of the filter width discussed earlier, are related to the fact that the orientation of the SFF vector in the eigenframe can be shown to be completely independent of the scalar field when using the Gaussian filter. In addition, sphere PDFs computed using the box filter (Fig. 4) are virtually identical to those computed using the Gaussian filter [Fig. 3(b)], both qualitatively and quantitatively. The reason for this behavior of $\boldsymbol{\tau}_\phi$ orientation, as well as that for its apparent independence from the filtered scalar field, is discussed in Sec. V A.

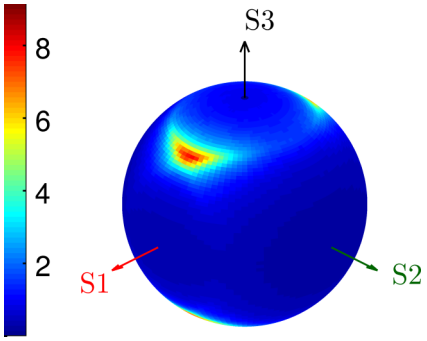

FIG. 4. (Color online) Alignment of $\boldsymbol{\tau}_\phi$ computed from case A using the box filter with $\kappa_c\eta = 1.6$ ($\kappa_c\eta_B = 0.1$).

IV. $\boldsymbol{\tau}_\phi$ ORIENTATION AND SUBFILTER MODELS

In this section, we compare the accuracy with which various SFF models, namely, the Smagorinsky model [4], the stretched vortex model [5], and the tensor-diffusivity model [8–11], predict $\boldsymbol{\tau}_\phi$ orientation when using a Gaussian filter. While not specifically designed for filtering in the viscous-convective subrange, it is still interesting to see whether possible extensions of the Smagorinsky and stretched vortex models would describe the orientation of the $\boldsymbol{\tau}_\phi$ vector well.

A. The Smagorinsky model

The Smagorinsky model is perhaps the most well-known and widely used subfilter model, given its conceptual simplicity and ease of implementation. The model relies on the concept of "eddy diffusivity":

$$\boldsymbol{\tau}_\phi = \mathcal{D}_t \nabla\widetilde{\phi}. \tag{8}$$

The dynamic Smagorinsky model [25] uses the idea of scale invariance for computing the turbulent diffusivity ($\mathcal{D}_t$) instead of prescribing a constant value but still relies on the filtered scalar gradient for determining vector direction.

B. The stretched vortex model

The stretched vortex model takes a more physical approach to model construction and works on the principle that convective scalar transport at the unresolved scales is accomplished by subfilter vortices [5]. Several simplifying assumptions lead to the following analytical form of the model:

$$(\tau_\phi)_i = C\left(\delta_{ij} - e_i^\omega e_j^\omega\right)\frac{\partial\widetilde{\phi}}{\partial x_j} \tag{9}$$

or

$$\boldsymbol{\tau}_\phi = C(\nabla\widetilde{\phi} - (\nabla\widetilde{\phi}\cdot\widehat{\boldsymbol{e}}_\omega)\widehat{\boldsymbol{e}}_\omega), \tag{10}$$

where $\widehat{\boldsymbol{e}}_\omega$ represents the unit vector in the direction of resolved vorticity, $\widetilde{\boldsymbol{\omega}}$. When filtering in the viscous-convective subrange ($\kappa_c\eta > 1.5$), the velocity field is fully resolved, i.e., $\widetilde{\boldsymbol{\omega}} = \boldsymbol{\omega}$. $\nabla\widetilde{\phi}$ and $\boldsymbol{\omega}$ tend to align in mutually orthogonal directions ($\widehat{\boldsymbol{e}}_3$ and $\widehat{\boldsymbol{e}}_2$, respectively), independent of the filtering kernel used.

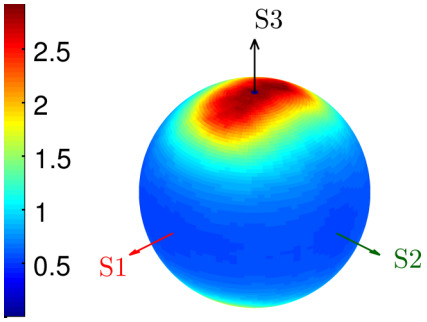

FIG. 5. (Color online) Alignment of $\nabla\widetilde{\phi}$ in the S_{ij} eigenframe, computed from case A using the Gaussian filter with $\kappa_c\eta = 1.6$ ($\kappa_c\eta_B = 0.1$).

This can be deduced by comparing Fig. 2(a) to Fig. 5, which shows the orientation of $\nabla\widetilde{\phi}$ computed using the Gaussian filter, with 95% of the scalar modes filtered out. The box and sharp-spectral filters yield similar results for $\nabla\widetilde{\phi}$ orientation. The orthogonality of $\nabla\widetilde{\phi}$ and $\boldsymbol{\omega}$ implies that the second term in Eq. (10) is essentially zero. An earlier formulation of the stretched vortex model for velocity modeling [26] uses an $\widehat{\boldsymbol{e}}_\omega$ that aligns with the subfilter vorticity, instead of the resolved vorticity. For this purpose the authors in Ref. [26] represent $\widehat{\boldsymbol{e}}_\omega$ as a linear combination of $\widehat{\boldsymbol{e}}_1$ and $\widehat{\boldsymbol{e}}_2$, both of which are perpendicular to $\nabla\widetilde{\phi}$. The dot product of $\nabla\widetilde{\phi}$ and $\widehat{\boldsymbol{e}}_\omega$ in Eq. (10) is zero even with this particular combination. Thus, whenever $\nabla\widetilde{\phi}$ and the assumed $\widehat{\boldsymbol{e}}_\omega$ are mutually orthogonal, the stretched vortex model reduces to a form resembling the Smagorinsky model [Eq. (8)], but with a different constant.

C. The tensor-diffusivity model

For sufficiently smooth velocity ($\boldsymbol{u}$) and scalar (ϕ) fields, and for a small filter-width Δ, the tensor-diffusivity model is evaluated from the leading order term in the Taylor-series expansion of Eq. (3). More precisely, the expansion takes the following form for a variety of filtering kernels, including the Gaussian and box filters [27,28]:

$$\begin{aligned}\boldsymbol{\tau}_\phi &= \widetilde{\boldsymbol{u}\phi} - \widetilde{\boldsymbol{u}}\widetilde{\phi} \\ &= C\nabla\widetilde{\boldsymbol{u}}\cdot\nabla\widetilde{\phi} + O(\Delta^4). \end{aligned} \tag{11}$$

The leading order term in Eq. (11) constitutes the tensor-diffusivity model. The coefficient C depends on the second moment $[\int_{-\infty}^{\infty} x^2 G(x)dx]$ of the filtering kernel and is identical for the forms of the Gaussian and box filtering kernels shown in Eqs. (5) and (6) ($C = \Delta^2/12$). This implies that, to leading order, $\boldsymbol{\tau}_\phi$ is virtually identical for both the Gaussian and box filters, which can be confirmed from Figs. 3(b) and 4. We note that moment integrals of the sharp-spectral kernel do not converge to finite values for order greater than 0. The consequence of using the sharp filter is discussed in greater detail in Sec. VI A. With the filter cutoff located in the viscous-convective subrange, $\nabla\widetilde{\boldsymbol{u}} = \nabla\boldsymbol{u}$, and Eq. (11) simplifies to

$$\boldsymbol{\tau}_\phi \approx \frac{\Delta^2}{12}\nabla\boldsymbol{u}\cdot\nabla\widetilde{\phi}. \tag{12}$$

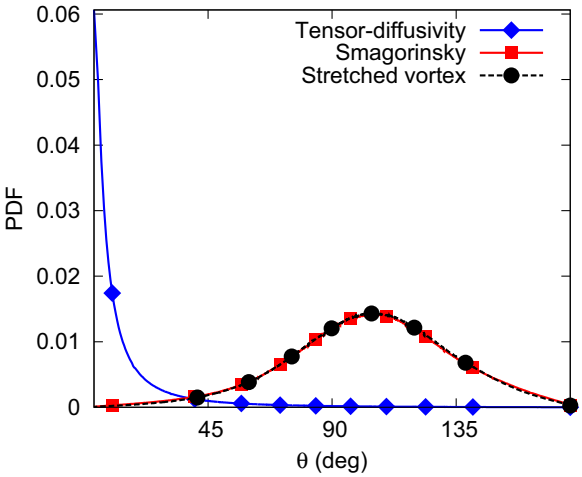

FIG. 6. (Color online) PDFs of the angle between the true SFF vector and the model predictions. Computed *a priori* from dataset B by filtering with the Gaussian filter at $\kappa_c\eta = 1.6$. The stretched vortex model depicted in this figure assumes alignment of $\widehat{\boldsymbol{e}}_\omega$ [Eq. (10)] with the resolved vorticity vector.

The higher order terms [$O(\Delta^4)$], which were neglected in the expression above, involve higher order velocity and scalar derivatives. In the viscous-convective subrange, scalar material elements have been speculated to experience effectively linear straining [1]. Under these conditions, it is appropriate to keep only the leading order term in Eq. (12).

D. Orientation predicted by the three subfilter models

To compare the effectiveness of the three models in predicting $\boldsymbol{\tau}_\phi$ orientation, we compute PDFs of the angles that the vectors defined by the three model terms [Eqs. (8), (10), and (12)] subtend with the vector defined by Eq. (3). The results shown in Fig. 6 indicate that the tensor-diffusivity model-predicted vector is co-aligned with the exact $\boldsymbol{\tau}_\phi$. However, both the Smagorinsky and stretched vortex model predictions are close to being counteraligned (i.e., orthogonal) with the SFF vector. These results are expected, as the filtered scalar gradient (which forms the basis of determining vector direction for the Smagorinsky and stretched vortex models) is aligned mainly with the $\widehat{\boldsymbol{e}}_3$ unit vector (Fig. 5), and the exact SFF term is close to zero in this direction (Fig. 3). Thus the Smagorinsky and stretched vortex models appear to be unsuitable representations for $\boldsymbol{\tau}_\phi$ when using the Gaussian filter. Similar results were found for all three models when using the box filter. Given the strong directional correlation between the exact $\boldsymbol{\tau}_\phi$ and the tensor-diffusivity model prediction, we conduct a detailed examination of the tensor-diffusivity model with regard to the strain-rate eigenframe.

V. STRAIN-RATE EIGENFRAME BASED ANALYSIS OF THE TENSOR-DIFFUSIVITY MODEL

The SFF vector computed from filtered DNS data [Eq. (3)] shows a very strong preference for alignment at a particular angle in the S_1-S_3 plane, when using the Gaussian or box filtering kernels (Figs. 3 and 4). This dependence can be

explained by analyzing the tensor-diffusivity model [8–11] for scalar transport. A similar analysis was carried out by Higgins *et al.* [20] regarding subfilter heat flux orientation in atmospheric measurement data. The authors found $\boldsymbol{\tau}_\phi$ to lie in the plane spanned by the mixed model, i.e., the tensor-diffusivity model combined with the Smagorinsky model. However, we show that the orientation of $\boldsymbol{\tau}_\phi$ in simulation data can be predicted exactly by the tensor-diffusivity model alone.

A. Explanation for orientation

To examine the reason for S_1-S_3 orientation of $\boldsymbol{\tau}_\phi$, the velocity gradient tensor ($\boldsymbol{\nabla u}$) in Eq. (12) is decomposed [20] into its symmetric and antisymmetric parts, i.e., the strain-rate tensor $S_{ij} = 1/2(u_{i,j} + u_{j,i})$ and the rotation tensor $\Omega_{ij} = 1/2(u_{i,j} - u_{j,i})$:

$$\boldsymbol{\tau}_\phi = \frac{\Delta^2}{12}(\boldsymbol{S} + \boldsymbol{\Omega}) \cdot \boldsymbol{\nabla}\widetilde{\phi} \tag{13}$$

$$= \frac{\Delta^2}{12}\boldsymbol{S} \cdot \boldsymbol{\nabla}\widetilde{\phi} + \frac{\Delta^2}{24}\boldsymbol{\omega} \times \boldsymbol{\nabla}\widetilde{\phi}. \tag{14}$$

Furthermore, from the Taylor-series expansion [29] of $\boldsymbol{\nabla}\widetilde{\phi}$ (for the Gaussian and box filters):

$$\boldsymbol{\nabla}\widetilde{\phi} = \boldsymbol{\nabla}\phi + \frac{\Delta^2}{24}\nabla^2(\boldsymbol{\nabla}\phi) + \cdots, \tag{15}$$

the filtered scalar gradient resembles the unfiltered gradient, which is the leading order term. We can confirm that the orientation of $\boldsymbol{\nabla}\widetilde{\phi}$ is virtually identical to that of the unfiltered $\boldsymbol{\nabla}\phi$, albeit with a slight drop in the maximum normalized PDF value, by comparing Figs. 5 and 2(b).

Using the observed alignment of $\boldsymbol{\omega}$ [Fig. 2(a)] and $\boldsymbol{\nabla}\widetilde{\phi}$ in the eigenframe (Fig. 5), we make the following simplifications:

$$\boldsymbol{\omega} = \pm|\boldsymbol{\omega}|\,\widehat{e}_2, \tag{16}$$

$$\boldsymbol{\nabla}\widetilde{\phi} = \pm|\boldsymbol{\nabla}\widetilde{\phi}|\,\widehat{e}_3, \tag{17}$$

where $\widehat{e}_2$ is the unit vector in the direction of axis S_2 and $\widehat{e}_3$ is the unit vector for S_3. Equation (14) can then be interpreted as follows:

$$\boldsymbol{\tau}_\phi \approx \frac{\Delta^2}{12}\left(\pm\boldsymbol{S} \cdot |\boldsymbol{\nabla}\widetilde{\phi}|\,\widehat{\boldsymbol{e}}_3 \pm \frac{1}{2}|\boldsymbol{\omega}|\,\widehat{\boldsymbol{e}}_2 \times |\boldsymbol{\nabla}\widetilde{\phi}|\,\widehat{\boldsymbol{e}}_3\right) \tag{18}$$

$$\approx \pm\frac{\Delta^2}{12}|\boldsymbol{\nabla}\widetilde{\phi}|\left(\lambda_3\,\widehat{\boldsymbol{e}}_3 \pm \frac{1}{2}|\boldsymbol{\omega}|\,\widehat{\boldsymbol{e}}_1\right). \tag{19}$$

As is evident from Eq. (19), $\boldsymbol{\tau}_\phi$ has measurable components only in the S_1 and S_3 directions. This explains the strong aversion to alignment in the S_2 direction (Figs. 3 and 4). Equation (19) also explains the enstrophy dependence of $\boldsymbol{\tau}_\phi$ orientation observed in Ref. [30]. In regions of low enstrophy ($|\boldsymbol{\omega}|^2/2$), the $\widehat{\boldsymbol{e}}_3$ component of Eq. (19) is dominant, which results in $\boldsymbol{\tau}_\phi$ aligning with the S_3 eigenvector.

Equation (19) can further be used to extract deterministic information about $\boldsymbol{\tau}_\phi$ orientation in the S_1-S_3 plane.

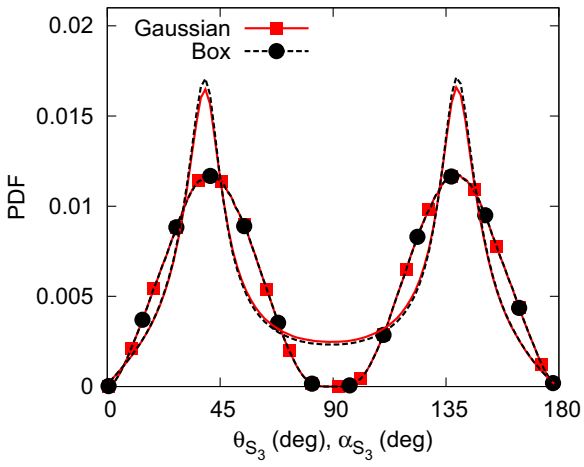

FIG. 7. (Color online) PDFs of θ_{S_3} (lines with symbols) and α_{S_3} (lines without symbols), computed pointwise from dataset B. Results shown for both Gaussian (solid lines) and box (broken lines) filters at $\kappa_c\eta = 1.6$.

The tensor-diffusivity model-predicted SFF vector [Eq. (19)] makes an angle of

$$\theta_{S_3} = \arctan\left(\pm\frac{|\boldsymbol{\omega}|}{2\lambda_3}\right) \tag{20}$$

with the S_3 axis, whereas the exact $\boldsymbol{\tau}_\phi$ [Eq. (3)] subtends the following angle:

$$\alpha_{S_3} = \arccos\left(\frac{\boldsymbol{\tau}_\phi \cdot \widehat{\boldsymbol{e}}_3}{|\boldsymbol{\tau}_\phi||\widehat{\boldsymbol{e}}_3|}\right). \tag{21}$$

The PDFs of θ_{S_3} and α_{S_3} computed from dataset B are plotted in Fig. 7. The distribution predicted by the tensor-diffusivity model, i.e., the PDF of θ_{S_3}, matches that of α_{S_3} quite well. The peaks in the PDFs occur at approximately 40° and 140°, which compares well with the θ_P values shown in Table II. Thus, the four symmetric orientation angles resulting from Eq. (20), specifically, $\pm|\theta_{S_3}|$ and $\pi \pm |\theta_{S_3}|$, are in excellent agreement with the sphere PDFs shown in Figs. 3 and 4. Overall, the numerical results support the analytical form of $\boldsymbol{\tau}_\phi$ given by Eq. (19), when using the Gaussian and box filters.

The complete independence of the angle in Eq. (20) from any scalar-field-related variable explains the Schmidt number and filter-width independence of the orientation of $\boldsymbol{\tau}_\phi$ observed in Sec. III. The orientation only depends on velocity-dependent variables, $\boldsymbol{\omega}$ and λ_3, which are largely unaffected by filtering for $\kappa_c\eta \geqslant 1.5$. However, the magnitude of $\boldsymbol{\tau}_\phi$ *will* depend on the filtered scalar field, as is clearly evident from the presence of $|\boldsymbol{\nabla}\widetilde{\phi}|$ in Eq. (19). The observations in this section confirm that the tensor-diffusivity model provides an excellent means of representing the subfilter-scale scalar-flux vector orientation analytically, when using the Gaussian or box filters.

B. Numerical stability of the tensor-diffusivity model

Although the tensor-diffusivity model provides close to an exact analytical form for the subfilter term, *a posteriori* implementation for velocity modeling in LES has been known to give rise to stability issues [29,31,32]. More precisely,

insufficient subfilter dissipation caused by the presence of negative viscosity in the model can result in the solution going unstable [10]. A common approach is to restore stability by augmenting the tensor-diffusivity model with a Smagorinsky term [29,31,32], which provides additional subfilter dissipation to compensate for the occurrence of negative viscosity. Other attempts to restore stability rely on either clipping negative viscosity [33] or incorporating regularization specific to the numerical method used [34]. In contrast to these issues, certain studies have noted that the tensor-diffusivity model by itself can lead to stable solutions, without augmentation with an additional dissipative term [29]. However, the subfilter dissipation was found to be insufficient in those cases, giving rise to inaccurate results. It is important to note that most of the *a posteriori* studies that observed solution instability were concerned with modeling the subfilter velocity stress tensor ($\boldsymbol{\tau_u}$), not the subfilter scalar-flux vector ($\boldsymbol{\tau}_\phi$). One exception is Ref. [34] which discusses *a posteriori* implementation for scalar transport, albeit in laminar one- and two-dimensional (1D and 2D) test cases.

Fortunately, the occurrence of negative diffusivity may not be a dominant issue when using the tensor-diffusivity model for scalar transport in homogeneous isotropic turbulence. More specifically, the tensor-diffusivity model may lead to stable results when used in the viscous-convective subrange. We can arrive at this conclusion by inspecting the subfilter dissipation ($\chi_{\boldsymbol{\tau}_\phi}$) of the filtered scalar variance. The filtered scalar transport equation, Eq. (2), is multiplied by the filtered scalar ($\widetilde{\phi}$), and in conjunction with the incompressibility condition ($\boldsymbol{\nabla}\cdot\boldsymbol{u}=0$), yields

$$\frac{\partial\widetilde{\phi}^2}{\partial t}+\boldsymbol{\nabla}\cdot(\widetilde{\boldsymbol{u}}\widetilde{\phi}^2)=\mathcal{D}\nabla^2\widetilde{\phi}^2-2\mathcal{D}|\boldsymbol{\nabla}\widetilde{\phi}|^2-2\boldsymbol{\nabla}\cdot(\widetilde{\phi}\boldsymbol{\tau}_\phi)+2\boldsymbol{\nabla}\widetilde{\phi}\cdot\boldsymbol{\tau}_\phi. \tag{22}$$

Here, $\widetilde{\chi}=2\mathcal{D}|\boldsymbol{\nabla}\widetilde{\phi}|^2$ and $\chi_{\boldsymbol{\tau}_\phi}=-2\boldsymbol{\nabla}\widetilde{\phi}\cdot\boldsymbol{\tau}_\phi$ are the resolved and unresolved scalar dissipation rates, respectively. $\chi_{\boldsymbol{\tau}_\phi}$ is responsible for scalar variance dissipation by the subfilter terms. Recalling that the scalar gradient vector shows strong preference for alignment with the $\widehat{\boldsymbol{e}}_3$ vector, and using Eq. (14), the subfilter scalar dissipation takes the following form:

$$\chi_{\boldsymbol{\tau}_\phi}\approx-\frac{\Delta^2}{6}\boldsymbol{\nabla}\widetilde{\phi}\cdot\left(\widetilde{\boldsymbol{S}}\cdot\boldsymbol{\nabla}\widetilde{\phi}+\frac{1}{2}\widetilde{\boldsymbol{\omega}}\times\boldsymbol{\nabla}\widetilde{\phi}\right) \tag{23}$$

$$\approx-\lambda_3|\boldsymbol{\nabla}\widetilde{\phi}|^2\frac{\Delta^2}{6}. \tag{24}$$

Using the fact that λ_3 is negative, Eqs. (22) and (24) indicate that the tensor-diffusivity model should always act as a sink for the resolved scalar variance. The absence of a positive λ_1 term, which would act as a positive source for scalar variance, negates the issue of negative diffusivity contributing to scalar variance increase.

We note, however, that Eq. (17) is a simplification since, in addition to the $\widehat{\boldsymbol{e}}_3$ component of $\boldsymbol{\nabla}\widetilde{\phi}$, there is a minimal spread in the $\widehat{\boldsymbol{e}}_1$ direction (Fig. 5). Nevertheless, dissipation caused by the λ_3 term [Eq. (24)] should dominate the minimal backscatter related to the minuscule $\widehat{\boldsymbol{e}}_1$ component of $\boldsymbol{\nabla}\widetilde{\phi}$. Thus, it should be possible to use the tensor-diffusivity model for scalar transport in homogeneous turbulence, without implementing extraneous means of restoring stability. This conjecture requires *a posteriori* testing, which is out of the scope of the current work.

We close the discussion on solution stability by noting that backscatter is a physically appropriate phenomenon associated with the stretching of material elements (Fig. 1) and is one of the several ways in which the small scales affect the large scales in turbulent flows [35]. In terms of scalar energy-transfer in spectral-space [3], backscatter represents an increase in variance at large scales due to deposition of energy by the small scales. Thus, solution stability permitting, subfilter models should try to account for backscatter whenever possible. This is another advantage that the tensor-diffusivity model offers over eddy-diffusivity based models, which are unable to account for backscatter inherently.

VI. DISCUSSION

A. Effect of filter shape

The discussion up until now has been concerned only with using the Gaussian and box filters when examining $\boldsymbol{\tau}_\phi$ orientation. In this section, we inspect what effect, if any, using a different filtering kernel (i.e., a different filter shape) can have on the orientation. Figure 8 shows sphere PDFs of $\boldsymbol{\tau}_\phi$ computed for case A using the sharp-spectral filtering kernel. We observe a drastic change in the behavior of the SFF orientation, when compared with equivalent results from the Gaussian and box filters (Figs. 3 and 4). The SFF vector distribution in the eigenframe is close to being completely random (i.e., PDF value ≈ 1) with the sharp filter, an observation which persists for more than an order of magnitude variation in the filter cutoff (Fig. 8). PDF values obtained using the three different filtering kernels are provided in Table III, along with data relevant for comparing MSG and LS forced scalar fields (discussed in Sec. VI B). The quantitative data confirm significant differences that arise when using the Gaussian or box filters vs the sharp-spectral filter. These results suggest that the observed alignment of $\boldsymbol{\tau}_\phi$ does not have a physical significance, and is merely a mathematical outcome of the filtering operation.

Severe filter dependence of the correlation between model predicted and exact subfilter stress tensor ($\boldsymbol{\tau_u}$) has been observed in previous numerical [36,37] and experimental [33] studies. Thus, the current observations, combined with those available in the literature, provide strong support for the viewpoint that in order to get accurate results, filtering and modeling must be treated as a unified process [29,36–38], irrespective of whether the velocity or the scalar is being modeled.

In spite of very different orientation of $\boldsymbol{\tau}_\phi$ when using the sharp-spectral filter, the results discussed in Secs. III C and V remain broadly applicable, since the expansion in Eq. (11) is valid for a wide class of continuous and discrete filters with finite second moments [27,28]. We reiterate that Eq. (11) is not valid when using the sharp-spectral filtering kernel, since the second moment of the sharp filter does not converge to a finite value. Thus, the tensor-diffusivity model may not perform

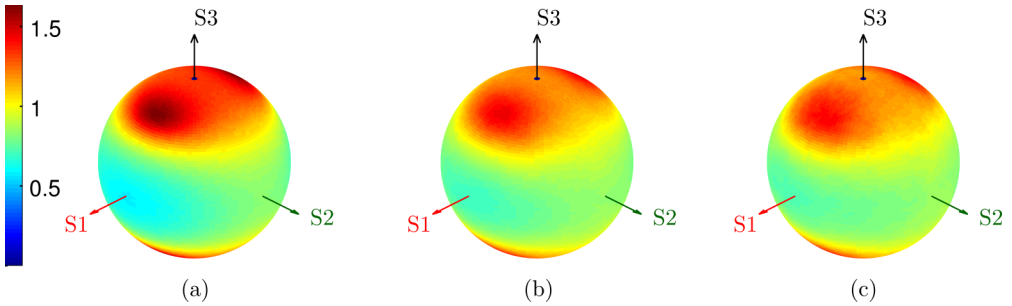

FIG. 8. (Color online) Similar to Fig. 3, but computed using the sharp-spectral filter. (a)$\kappa_c\eta = 10$, $\kappa_c\eta_B = 0.625$; (b)$\kappa_c\eta = 1.6$, $\kappa_c\eta_B = 0.1$; (c) $\kappa_c\eta = 0.8$, $\kappa_c\eta_B = 0.05$.

well in predicting $\boldsymbol{\tau}_\phi$ orientation when coupled with the sharp filter.

B. Effect of scalar forcing

The $\boldsymbol{\tau}_\phi$ distributions discussed in Secs. III C and V were computed for a scalar field forced by imposing a mean scalar gradient (MSG) [15]. Identical computations were carried out for a scalar field mimicking the dynamics of decaying scalar fluctuations (linear scalar forcing [16]). The alignment trends observed were identical in both cases (Table III), even though the means of sustaining small scale fluctuations, and consequently, the scalar variance spectra, have been seen to differ at high Schmidt numbers [16]. The indifference of $\boldsymbol{\tau}_\phi$ orientation to the forcing method is reminiscent of the Schmidt number and filter-width independence observed in Sec. III C, and may yet again be explained using the absence of a $\widetilde{\phi}$-dependent term in Eq. (20).

C. Implications for practical LES

The present results indicate that model selection for practical LES must be strongly contingent on the effective filtering kernel used. This raises a few crucial questions, particularly: (1) Is it appropriate to use implicit filtering in LES? (2) Is it appropriate to think of subfilter terms as being entirely physical in nature, rather than to consider their combined physical and mathematical role? Both these questions are of critical relevance to practical LES, where implicit filtering (not to be confused with implicit LES [39]) and filter-independent model selection are common approaches.

Implicit filtering removes high wave-number spatial fluctuations by projecting the solution on to a coarse grid, which contrasts with explicit filtering where the solution is convolved with a filtering kernel. Projection on a coarse grid, when using spectral methods in LES, is equivalent to filtering with a sharp-spectral filter. The use of finite-volume and finite-difference schemes may introduce yet another level of filtering, which may not be well-defined mathematically [37,40–43]. Thus, relying on implicit filtering can result in very poor correlation of the model predicted and exact SFF terms, which can be detrimental to solution accuracy. In this regard, explicit filtering has been considered in the literature as a means of introducing some measure of predictability into the behavior of subfilter terms, in addition to providing control over discretization errors. More specifically Refs. [27,29] use explicit filtering to ensure strong correlation between the subfilter terms and the models used, and Refs. [41–43] note a reduction in numerical error (along with a tendency to obtain grid-independent results) when using explicit filtering.

The second question posed is concerned with the fact that there is a prevalent tendency to view the subfilter term as being physical in nature, and the choice of a particular model for LES

TABLE III. Case A ($\mathrm{Re}_\lambda = 30$, $\mathrm{Sc} = 256$). Comparison of alignment data for different filtering kernels, and for MSG and LS forcing. The ranges of accuracy for θ_P and θ_A are $\pm 0.9^\circ$ and $\pm 1.8^\circ$, respectively.

		MSG			LS		
Filter	PDF	$\kappa_c\eta = 10$	$\kappa_c\eta = 1.6$	$\kappa_c\eta = 0.8$	$\kappa_c\eta = 10$	$\kappa_c\eta = 1.6$	$\kappa_c\eta = 0.8$
Gaussian	min	0.15	0.17	0.18	0.15	0.18	0.20
	max	9.14	7.32	5.77	9.03	7.09	5.48
	θ_P	42.3°	42.3°	42.3°	42.3°	42.3°	42.3°
	θ_A	5.4°	1.8°	5.4°	5.4°	5.4°	1.8°
Box	min	0.15	0.17	0.17	0.15	0.18	0.20
	max	9.23	7.88	6.42	9.10	7.64	6.03
	θ_P	42.3°	42.3°	40.5°	42.3°	42.3°	42.3°
	θ_A	5.4°	5.4°	1.8°	5.4°	5.4°	1.8°
Sharp-spectral	min	0.29	0.35	0.36	0.29	0.36	0.37
	max	1.63	1.46	1.44	1.63	1.43	1.42
	θ_P	35.1°	36.9°	35.1°	35.1°	35.1°	33.3°
	θ_A	1.8°	1.8°	9°	1.8°	5.4°	9°

is often made independently of the implicit or explicit filter used [36]. The filter dependence of subfilter terms suggests that there is a dominant mathematical aspect involved in modeling, which must not be ignored. Thus, modeling and filtering must be treated as a unified process by using appropriate model-filter combinations in LES.

VII. CONCLUSION

In this paper, we have examined the alignment behavior of the subfilter-scale scalar-flux vector in the eigenframe of the strain-rate tensor. The focus is placed on filtering in the viscous-convective subrange. Results obtained from filtered DNS datasets indicate strong preferential alignment of the SFF vector ($\boldsymbol{\tau}_\phi$) in a particular direction, when using both the Gaussian and box filters. The alignment direction is explained by analyzing the tensor-diffusivity model, based on the observed preferential orientation of the vorticity ($\boldsymbol{\omega}$) and scalar gradient ($\nabla\widetilde{\phi}$) vectors. The independence of the SFF vector orientation from the filter width, the flow Schmidt number, and the scalar-forcing method, is explained by extracting the orientation angle from the tensor-diffusivity model. The relevant orientation angle, θ_{S_3}, is shown to depend only on velocity-related variables, $\boldsymbol{\omega}$ and λ_3. The remarkable agreement between numerical results and those predicted by the tensor-diffusivity model confirms that it provides close to an exact analytical form for the subfilter term, when using the Gaussian or box filtering kernels.

Using the orientation of $\nabla\widetilde{\phi}$ in the strain-rate eigenframe, it is shown that the subfilter dissipation term for the tensor-diffusivity model acts predominantly as a sink for the scalar variance. Thus, the issue of solution instability induced by the occurrence of negative diffusivity may not arise when using the model for scalar transport in homogeneous isotropic turbulence. This result should remain valid, at least, as long as the filter width is located in the viscous-convective subrange.

Analyzing the effect of filter shape indicates close to random orientation of the SFF vector when using the sharp-spectral filter. Such strong dependence of the subfilter term on filter shape raises concern regarding the suitability of using implicit filtering in LES, which is often the preferred method of choice for such simulations. Additionally, comparison of various SFF models indicates that the tensor diffusivity is capable of predicting $\boldsymbol{\tau}_\phi$ orientation quite accurately when using the Gaussian and box filters, whereas the Smagorinsky and stretched vortex models do not perform well in this regard.

The results reinforce the viewpoint that filtering and modeling must be tackled as a unified issue in LES, and appropriate filter-model combinations must be used. The observed filter dependence also suggests that it may not be appropriate to ascribe a solely physical role to subfilter models, and that it is more pertinent to examine their combined physical and mathematical role in LES.

ACKNOWLEDGMENT

The authors gratefully acknowledge support from the US Department of Energy–Basic Energy Sciences Division (DE-SC0006591), which included access to computational resources at the National Energy Research Scientific Computing Center (NERSC). We also thank Prof. Yeung, whose datasets were invaluable in the conceptual stage of the analysis. Professor Balarac's cooperation was crucial in implementing the low wave-shell velocity forcing scheme used in this study. The authors also benefited from helpful discussions with Professors Leonard and Meiron.

[1] G. K. Batchelor, J. Fluid Mech. **5**, 113 (1959).
[2] G. C. Burton, Phys. Fluids **20**, 035103 (2008).
[3] S. Verma and G. Blanquart, Phys. Fluids **25**, 055104 (2013).
[4] J. Smagorinsky, Mon. Wea. Rev. **91**, 99 (1963).
[5] D. I. Pullin, Phys. Fluids **12**, 2311 (2000).
[6] J. Bardina, J. H. Ferziger, and W. C. Reynolds, AIAA Paper 80–1357, 1980.
[7] J. Bardina, J. H. Ferziger, and W. C. Reynolds, Stanford University Report No. TF-19, 1983.
[8] A. Leonard, Adv. Geophys. **18**, 237 (1975).
[9] R. A. Clark, J. H. Ferziger, and W. C. Reynolds, J. Fluid Mech. **91**, 1 (1979).
[10] A. Leonard, AIAA Paper 97–0204, 1997.
[11] K. W. Bedford and W. K. Yeo, in *Large Eddy Simulation of Complex Engineering and Geophysical flows*, edited by B. Galperin and S. A. Orszag (Cambridge University Press, Cambridge, United Kingdom, 1993), pp. 513–537.
[12] O. Desjardins, G. Blanquart, G. Balarac, and H. Pitsch, J. Comput. Phys. **227**, 7125 (2008).
[13] R. R. Nourgaliev and T. G. Theofanous, J. Comput. Phys. **224**, 836 (2007).
[14] K. Alvelius, Phys. Fluids **11**, 1880 (1999).
[15] M. R. Overholt and S. B. Pope, Phys. Fluids **8**, 3128 (1996).
[16] P. L. Carroll, S. Verma, and G. Blanquart, Phys. Fluids **25**, 095102 (2013).
[17] P. K. Yeung, S. Xu, D. A. Donzis, and K. R. Sreenivasan, Flow Turbul. Combust. **72**, 333 (2004).
[18] S. A. Orszag, J. Atmos. Sci. **28**, 1074 (1971).
[19] W. T. Ashurst, A. R. Kerstein, R. M. Kerr, and C. H. Gibson, Phys. Fluids **30**, 2343 (1987).
[20] C. W. Higgins, M. B. Parlange, and C. Meneveau, Geophys. Res. Lett. **31**, 1 (2004).
[21] A. Tsinober, E. Kit, and T. Dracos, J. Fluid Mech. **242**, 169 (1992).
[22] C. W. Higgins, M. B. Parlange, and C. Meneveau, Bound.-Lay. Meteorol. **109**, 59 (2003).
[23] P. E. Hamlington, J. Schumacher, and W. J. A. Dahm, Phys. Rev. E **77**, 026303 (2008).
[24] P. E. Hamlington, J. Schumacher, and W. J. A. Dahm, Phys. Fluids **20**, 111703 (2008).
[25] M. Germano, U. Piomelli, P. Moin, and W. H. Cabot, Phys. Fluids A **3**, 1760 (1991).
[26] A. Misra and D. I. Pullin, Phys. Fluids **9**, 2443 (1997).
[27] D. Carati, G. S. Winckelmans, and H. Jeanmart, J. Fluid Mech. **441**, 119 (2001).

[28] C. D. Pruett, J. S. Sochacki, and N. A. Adams, Phys. Fluids **13**, 2578 (2001).
[29] G. S. Winckelmans, A. A. Wray, O. V. Vasilyev, and H. Jeanmart, Phys. Fluids **13**, 1385 (2001).
[30] S. G. Chumakov, Phys. Rev. E **78**, 036313 (2008).
[31] B. Vreman, B. Geurts, and H. Kuerten, Theor. Comp. Fluid Dyn. **8**, 309 (1996).
[32] B. Vreman, B. Geurts, and H. Kuerten, J. Fluid Mech. **339**, 357 (1997).
[33] S. Liu, C. Meneveau, and J. Katz, J. Fluid Mech. **275**, 83 (1994).
[34] P. Moeleker and A. Leonard, J. Comput. Phys. **167**, 1 (2001).
[35] J. A. Domaradzki and E. M. Saiki, Theor. Comp. Fluid Dyn. **9**, 75 (1997).
[36] U. Piomelli, P. Moin, and J. H. Ferziger, Phys. Fluids **31**, 1884 (1988).
[37] G. De Stefano and O. V. Vasilyev, Phys. Fluids **14**, 362 (2002).
[38] C. D. Pruett and N. A. Adams, Phys. Fluids **12**, 1133 (2000).
[39] L. G. Margolin and W. J. Rider, Int. J. Numer. Meth. Fluids. **39**, 821 (2002).
[40] R. S. Rogallo and P. Moin, Ann. Rev. Fluid Mech. **16**, 99 (1984).
[41] T. S. Lund, Comput. Math. Appl. **46**, 603 (2003).
[42] S. T. Bose, P. Moin, and D. You, Phys. Fluids **22**, 105103 (2010).
[43] O. V. Vasilyev, T. S. Lund, and P. Moin, J. Comput. Phys. **146**, 82 (1998).